Inorganic Chemistry

Article

pubs.acs.org/IC

Enhanced Thermoelectric Figure of Merit in Stannite–Kuramite Solid Solutions $Cu_{2+x}Fe_{1-x}SnS_{4-y}$ (x = 0–1) with Anisotropy Lowering

Yosuke Goto,*[,†] Fumihiko Naito,[†] Rina Sato,[†] Keigo Yoshiyasu,[†] Takanori Itoh,[‡] Yoichi Kamihara,[†] and Masanori Matoba[†]

[†]Department of Applied Physics and Physico-Informatics, Faculty of Science and Technology, Keio University, 3-14-1 Hiyoshi, Yokohama 223-8522, Japan

[‡]Quality Management Group, AGC Seimichemical Company, Ltd., 3-2-10 Chigasaki, Chigasaki City, Kanagawa 253-8585, Japan

Supporting Information

ABSTRACT: In this Article, we elucidate the structural and thermoelectric properties of stannite–kuramite solid solutions, $Cu_{2+x}Fe_{1-x}SnS_{4-y}$ (x = 0–1), with sulfur defects (y) ≤ 0.4. Structural analysis revealed that anisotropy decreases and Cu/Sn disorder increases with an increase in x. The samples with x = 0.8–1 exhibit degenerate conduction, whereas the Seebeck coefficient (S) remains relatively high, $S \approx 100\ \mu V\ K^{-1}$ for x = 0.8 at 300 K. Thermal conductivities (κ) of the solid solutions are in the range 10^{-3}–10^{-2} W cm^{-1} K^{-1}, which is close to the κ value of silicon dioxide. The dimensionless figure of merit (ZT) reaches 0.044 for x = 0.8 at 300 K. The ZT is enhanced significantly by an increase in temperature and is doubly larger than that of x = 0 at 300 K. These findings allow us to attain higher ZT values through optimization of chemical composition.

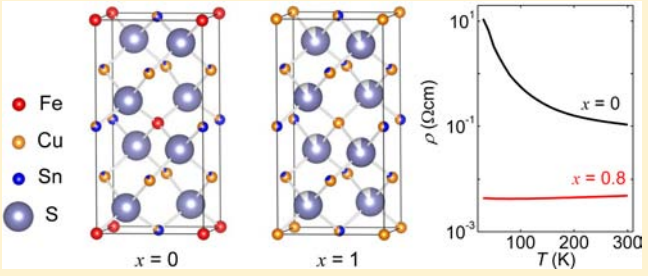

INTRODUCTION

Thermoelectrics is a direct conversion technique of heat to electric power using conductors and/or degenerated semiconductors that have temperature gradients.[1−3] Waste heat energy harvesting using this technique is a main goal for future applications. A thermoelectric material is evaluated by the dimensionless figure of merit $ZT = S^2T/\rho\kappa$, where T is the absolute temperature, S is the Seebeck coefficient, ρ is the electrical resistivity, and κ is the thermal conductivity. In a simple kinetic picture, κ is given by the sum of contributions from the elastic vibrations of a lattice (phonon) κ_l and free electron Fermi gas κ_e.[4] A method to design thermoelectric materials is to optimize the transport properties of materials exhibiting both low κ_l and low ρ.[5] Skutterudites,[6] clathrates,[7] zinc antimonides,[8,9] cobalt oxides,[10] and copper chalcogenides[11,12] have all been reported as promising materials in thermoelectric technology. These compounds, which have site disorder and/or crystallographic deficiencies, exhibit high ZT probably because of the existence of disordered ions scattering phonons.

The thermoelectric properties of stannite-type compounds such as $Cu_2ZnSnSe_4$,[13] $Cu_2CdSnSe_4$,[14] Cu_3SbSe_4,[15] and $Cu_2ZnGeSe_4$[16] have recently been studied. These compounds, which have been mainly studied as possible photovoltaic materials,[17] have a high ZT because of their very low κ. Figure 1a shows the crystallographic structure of stannite (Cu_2FeSnS_4), which belongs to the tetragonal $I\bar{4}2m$ space group.[18] The unit cell is characterized by a superstructure of zinc-blende-type structures containing three different cations. Although many elemental combinations have been reported in stannite-type compounds, such as Cu_2–II–IV–VI_4 (II = Mn, Fe, Co, Ni, Cu, Zn, Sr, Ba, Cd, Hg; IV = Si, Ge, Sn; VI = S, Se),[19−26] thorough and systematic research has not been reported concerning their structural and thermoelectric properties.

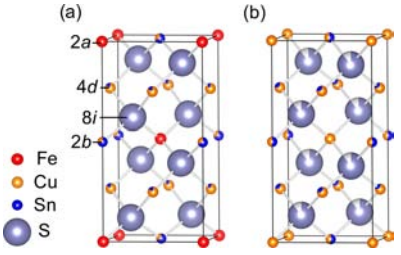

Figure 1. Crystallographic structures of $Cu_{2+x}Fe_{1-x}SnS_{4-y}$ [(a) x = 0 and (b) x = 1]. Sites denoted as 4d and 2b are partially occupied by Cu and Sn. Site occupancies were summarized in Table 2. The illustration was drawn on the basis of the structural model of stannite[18] and our results of structural refinement.

Kuramite (Cu_3SnS_4) is a stannite-type mineral.[27,28] The details of chemical substitution in stannite–kesterite (Cu_2ZnSnS_4) solid solutions are characterized by cation random distribution,[29,30] whereas those of stannite–kuramite solid solutions are still controversial. Mössbauer spectroscopy suggests Fe^{3+} atoms occupy the centers of octahedra formed by sulfur atoms;[31,32] on the other hand, X-ray absorption fine structure (XAFS) spectroscopy indicates the iron atoms are tetrahedrally coordinated by four sulfur atoms.[33]

Received: April 15, 2013
Published: August 9, 2013

   dx.doi.org/10.1021/ic401310c | Inorg. Chem. 2013, 52, 9861−9866

Table 1. Positional Parameters of $Cu_{2+x}Fe_{1-x}SnS_{4-y}$ in Rietveld Refinements

space group $I\bar{4}2m$ (No. 121) $\alpha = \beta = \gamma = 90°$			
atoms	sites	site occupancy	atomic coordinates (x, y, z)
Fe, Cu, Sn	2*a*	1	0, 0, 0
Cu, Sn	4*d*	1	0, 1/2, 1/4
Sn, Cu	2*b*	1	0, 0, 1/2
S	8*i*	~1	~0.25, ~0.25, ~0.125

In this study, we elucidate the structural and thermoelectric properties of stannite−kuramite solid solutions, $Cu_{2+x}Fe_{1-x}SnS_{4-y}$ (x = 0−1). Structural anisotropy decreases with x, and all samples are characterized by Cu/Sn disorder, which is quite different from stannite−kesterite solid solutions. The value of ρ decreases significantly when x = 0.8−1 and ZT reaches a doubly larger value than that of x = 0.

EXPERIMENTAL SECTION

Polycrystalline samples of $Cu_{2+x}Fe_{1-x}SnS_{4-y}$ (x = 0−1) were synthesized by solid-state reactions.[34,35] Stoichiometric ratios of Cu (Kojundo Chemical; 99.9%), Fe (Kojundo Chemical; 99.999%), Sn (Kojundo Chemical; 99.99%), and S (Kojundo Chemical; 99.99%) powders were heated at 750 °C for 96 h in an evacuated silica tube. The products were ground into powders and then pressed into pellets. The pellets were again heated at 750 °C for 40 h in an evacuated silica tube. After heat treatment, the samples were quenched in iced water.

Powder X-ray diffraction (XRD) patterns were collected using a Rigaku RINT 2500 with Cu Kα radiation (λ = 0.154060 nm). The crystallographic structure was refined by the Rietveld method using the RIETAN-FP code.[36] The crystal structures were visualized using the VESTA code.[37] The chemical composition of the samples, especially the amount of anion defects, was determined using an electron probe microanalyzer (EPMA; SHIMADZU EPMA-8705). The amounts of Cu, Fe, and S were quantified from Kα radiation, and the amount of Sn was quantified from Lα radiation. The accuracy of EPMA analysis was estimated at ~10%.

The value of ρ was measured by a four-probe technique using Au electrodes at temperatures 30−300 K. S and κ were measured from 80 to 300 K using a steady-state technique in a closed refrigerator pumped down to 10^{-3} Pa. The temperature gradient was monitored using copper-constantan thermocouples. The values of S and κ were calculated from $S = \Delta V \Delta T^{-1}$ and $\kappa = q\Delta T^{-1}$, respectively, where ΔV is the Seebeck voltage between the Cu wires, ΔT is the temperature difference between the thermocouples, which was controlled to be within the range 0−3 K by using a strain-gauge as a heater, and q is the heat flux density.

RESULTS

Figure 2 shows the powder XRD patterns of $Cu_{2+x}Fe_{1-x}SnS_{4-y}$ (x = 0 and 1). Almost all diffraction peaks can be assigned to those of the stannite phase, which indicates that this is the dominant phase in the samples. However, there are several weak peaks that can be attributed to SnO_2 or Cu_9S_5 impurities. The amounts of impurities in all samples are less than 7.4 and 3.4 mol % for SnO_2 or Cu_9S_5, respectively. The grain size is evaluated to be ~20 μm for x = 0, whereas grain boundaries are hardly observed for x = 1, as shown in the inset of Figure 2. The chemical composition of the samples obtained from EPMA analysis is summarized in Table S1. The x = 0 sample was used as the standard reference. The amounts of the three cations are consistent with nominal stoichiometric ratio while finite anion deficiency exists. The amounts of anion defects are evaluated to be ~10 mol % for x = 0.4−1.

Table 2 summarizes refined crystallographic parameters. Figure 3 shows the lattice parameters (a and c) versus x. These

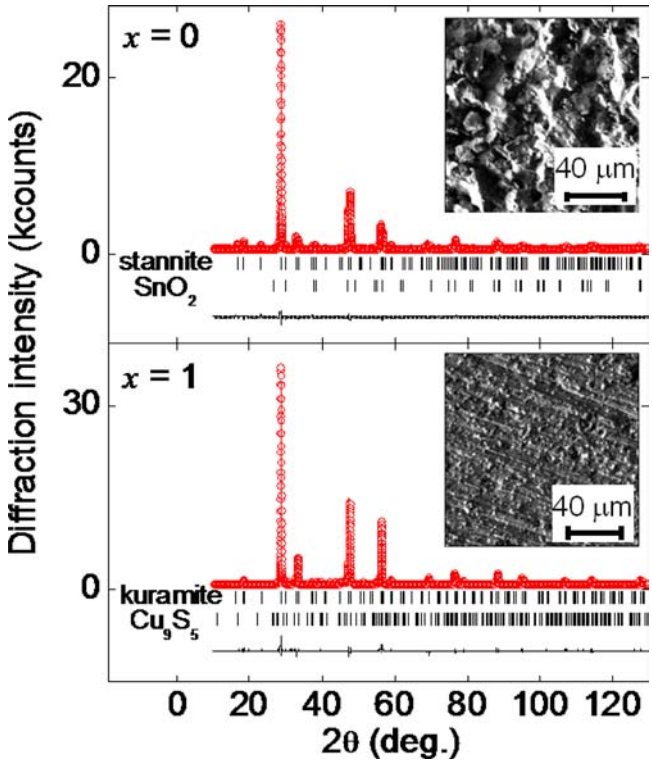

Figure 2. Observed (red ○) and calculated (red line) XRD profiles of $Cu_{2+x}Fe_{1-x}SnS_{4-y}$ (x = 0 and 1). The black line represents the difference between the observed and calculated profiles. The vertical marks represent the calculated Bragg diffraction position of stannite and impurity phase (SnO_2 or Cu_9S_5), respectively.

parameters for x = 0 and 1 are in agreement with previously reported values.[18,27,28] The value of a generally decreases, whereas the value of c increases as x increases in the range 0−0.6. However, the value of a exhibits a nonlinear trend. The discontinuity of lattice parameters has also been observed in the solid solutions $Cu_2Zn_{1-x}Fe_xSnS_4$[29,38] and $Cu_2Zn_{1-x}Fe_xGeSe_4$.[39] This non-Vegard like behavior should be ascribed to the cation random distribution, as described later. In stannite-type compounds, structural anisotropy is described by a tetragonal parameter, $c/2a$. The value of $c/2a$ is essentially constant at ~1 for x = 0.6−1, as shown in Figure 3, indicating a decrease of structural anisotropy in this range.

The cation site can be occupied with up to three cations, which were imposed the linear constraints to maintain their total occupancies in the nominal stoichiometric ratios.[30] The anomalous scattering of Fe allows us to determine the site occupancies of Cu and Fe using Cu Kα radiation, despite the similar electron number of these metals.[40,41] Figure 4 shows the site occupancies versus x, refined by the Rietveld analysis. Mixed occupation by Cu and Sn at the 4*d* and 2*b* sites was observed for x = 0, whereas the 2*a* site was occupied by Fe only. The Cu/Sn disorder in the 4*d* and 2*b* sites increases with x, while Fe on 2*a* site was continuously substituted with Cu.

As shown in Figure 5a, the bond lengths (r) for the three cation sites and anion converge at $r \approx 0.235(2)$ nm, indicating a decrease in structural anisotropy with increasing x. Figure 5b shows the bond valence sum (BVS) calculated from the structural data.[42,43] The BVS of Fe is 3.23 for x = 0, which is much larger than that expected from a simple ionic model of $Cu^{1+}{}_2Fe^{2+}Sn^{4+}S_4$,[44] suggesting that the Fe−S bond is under strong compression. The BVS of the 2*a* site decreases with an

dx.doi.org/10.1021/ic401310c | Inorg. Chem. 2013, 52, 9861−9866

Table 2. Refined Crystallographic Parameters and Reliability Factors of $Cu_{2+x}Fe_{1-x}SnS_{4-y}$ from Rietveld Refinements[a]

atoms (site)	parameters	$x = 0$	$x = 0.1$	$x = 0.2$	$x = 0.4$	$x = 0.6$	$x = 0.7$	$x = 0.8$	$x = 0.9$	$x = 1$
Fe, Cu, Sn ($2a$)	g_{Fe}	1	0.9	0.8	0.6	0.4	0.3	0.2	0.1	0
	g_{Cu}	0	0.1	0.2	0.4	0.556(15)	0.687(15)	0.8	0.9	1
	g_{Sn}	0	0	0	0	0.044	0.013	0	0	0
	U_{iso} (10^{-4} nm^2)	1.46(21)	3.74(27)	6.62(30)	7.21(30)	2.98(27)	2.64(30)	1.50(27)	0.64(3)	1.69(24)
Cu, Sn ($4d$)	g_{Cu}	0.848(3)	0.935(3)	0.879(3)	0.876(6)	0.846(6)	0.813(6)	0.805(6)	0.779(9)	0.759(6)
	g_{Sn}	0.152	0.065	0.121	0.124	0.154	0.187	0.195	0.221	0.241
	U_{iso} (10^{-4} nm^2)	2.35(15)	0.43(12)	1.00(3)	0.01(9)	1.36(12)	1.40(12)	1.14(12)	1.25(12)	1.73(12)
Sn, Cu ($2b$)	g_{Sn}	0.696	0.870	0.758	0.751	0.649	0.613	0.610	0.557	0.518
	g_{Cu}	0.304	0.130	0.242	0.249	0.351	0.387	0.390	0.443	0.482
	U_{iso} (10^{-4} nm^2)	1.21(9)	1.45(12)	1.78(12)	2.47(15)	1.09(12)	0.99(15)	0.74(12)	0.75(15)	0.63(12)
S ($8i$)	g	1	1	0.94	0.88	0.94	0.87	0.89	0.86	0.90
	x	0.2390(9)	0.2442(9)	0.2448(9)	0.2446(12)	0.2455(15)	0.2399(15)	0.2460(12)	0.2468(18)	0.2477(15)
	z	0.1131(6)	0.1197(6)	0.1106(6)	0.1143(9)	0.1217(15)	0.123(3)	0.1239(27)	0.125(9)	0.1271(18)
	U_{iso} (10^{-4} nm^2)	0.18(12)	0.70(9)	0.17(9)	0.68(15)	1.43(12)	1.22(15)	0.13(12)	0.13(12)	0.68(12)
	a and b (nm)	0.544312(24)	0.542559(12)	0.542746(15)	0.542421(12)	0.541803(9)	0.542624(18)	0.54247(18)	0.542598(21)	0.542247(21)
	c (nm)	1.07383(6)	1.07489(3)	1.07724(3)	1.07882(3)	1.08172(24)	1.08390(6)	1.08365(6)	1.08379(6)	1.08259(6)
	$r_{2a\ site-S}$ (nm)	0.2204(3)	0.2273(3)	0.2225(3)	0.2245(6)	0.2296(12)	0.2272(21)	0.2316(18)	0.233(3)	0.2345(9)
	$r_{4d\ site-S}$ (nm)	0.2423(3)	0.2376(3)	0.2437(3)	0.2413(6)	0.2365(9)	0.2364(21)	0.2355(18)	0.235(3)	0.2334(6)
	$r_{2b\ site-S}$ (nm)	0.2348(3)	0.2347(3)	0.2293(3)	0.2315(6)	0.2353(9)	0.2399(21)	0.2366(18)	0.237(3)	0.2374(6)
	R_{wp} (%)	5.07	5.72	5.42	6.60	6.52	6.37	5.20	5.99	5.00
	S	1.44	1.58	1.64	2.11	1.96	1.80	1.71	2.02	1.63
	R_B (%)	3.82	4.37	2.33	4.81	6.24	7.88	2.87	8.96	3.85
	R_F (%)	2.39	2.29	1.56	3.49	4.26	5.11	2.38	4.21	2.07

[a]Note that sulfur occupancies on $8i$ site were fixed at EPMA results. g, site occupancy; U_{iso}, isotropic atomic displacement parameter; r, bond length; R_{wp}, the reliability weighted pattern factors; S, the GOF factors ($=R_{wp}/R_e$, R_e, the reliability expected factor); R_B, the reliability Bragg factor; R_F, the reliability structure factor.

dx.doi.org/10.1021/ic401310c | Inorg. Chem. 2013, 52, 9861−9866

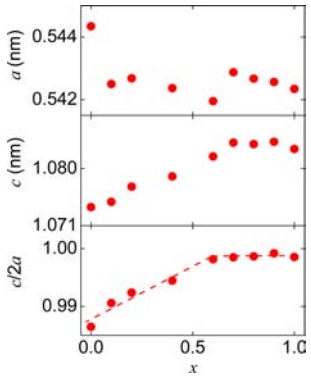

Figure 3. Lattice parameters (a and c) and ratio of $c/2a$ of $Cu_{2+x}Fe_{1-x}SnS_{4-y}$. The dashed line shows the guide to the eyes.

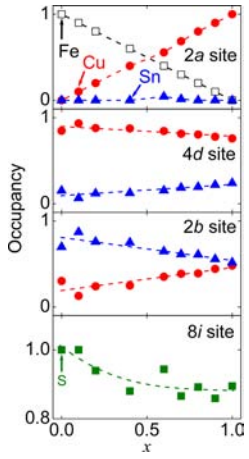

Figure 4. Site occupancies of $Cu_{2+x}Fe_{1-x}SnS_{4-y}$. Cation occupancies were obtained from Rietveld analysis, while anion occupancies were taken from EPMA analysis.

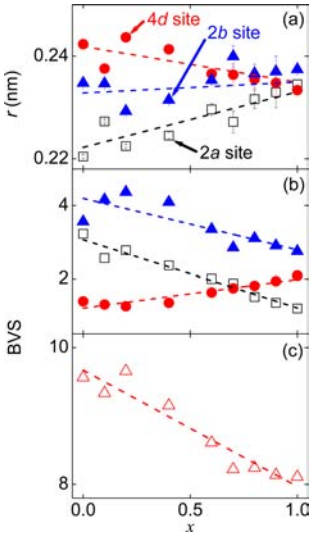

Figure 5. (a) Bond length (r) between three cation sites and anion, (b) bond valence sum (BVS), and (c) total BVS of $Cu_{2+x}Fe_{1-x}SnS_{4-y}$. The dashed line shows the guide to the eyes.

increase in x, resulting in a value of 1.20 for $x = 1$. The BVS of the 4d site increases from 1.39 to 2.08, whereas that of the 2b site decreases from 3.56 to 2.75. This can be attributed to the increase in mixed occupation between Cu^{1+} and Sn^{4+} in the 4d and 2b sites with increasing x. Figure 5c shows the total BVS (BVS_{tot}), which is defined as follows:

$$BVS_{tot} = BVS_{2a} + 2\cdot BVS_{4d} + BVS_{2b} \quad (1)$$

where BVS_i ($i = 2a$, 4d, and 2b) denotes the BVS of the i site. The BVS_{tot} decreases from 9.57 to 8.11, which is consistent with the anion defect increasing with x (see Figure 4).

Figure 6 shows the transport properties at $x = 0$, 0.7, 0.8, and 1. Figure 6a shows ρ versus T. The magnitude of ρ is 10^{-1} Ω cm at

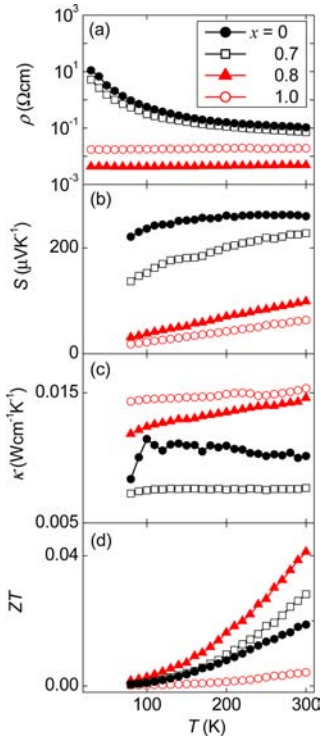

Figure 6. Thermoelectric properties of $Cu_{2+x}Fe_{1-x}SnS_{4-y}$ ($x = 0$, 0.7, 0.8, and 1). (a) Electrical resistivity (ρ) versus temperature (T), (b) Seebeck coefficient (S) versus T, (c) thermal conductivity (κ) versus T, and (d) dimensionless figure of merit (ZT) versus T.

300 K, and the activation energy (E_a) is calculated as ~0.02 eV for $x = 0$. A negative temperature coefficient ($d\rho/dT < 0$) is present until $x = 0.7$, and E_a is in the range 0.02−0.05 eV. The value of ρ drastically drops, and a slightly positive temperature coefficient ($d\rho/dT > 0$) is observed for $x = 0.8$−1, indicating that these compounds are degenerate semiconductors. The magnitude of ρ at 300 K decreases to 10^{-3} Ω cm for $x = 0.8$. Figure 6b shows S versus T. A positive value of S was obtained for all samples, indicating these compounds are p-type semiconductors. The Seebeck coefficient for metals or degenerate semiconductors with parabolic band and energy-dependent scattering approximation is given[45] by:

$$S = \frac{8\pi^2 k_B^2}{3eh^2} m^* T \left(\frac{\pi}{3n}\right)^{2/3}$$

where n is the carrier concentration, and m^* is the effective mass of the carrier. As expected from the $\rho-T$ plot, the value of S at 300 K is in the range 170−330 μV K^{-1} for $x = 0$−0.7, and it decreases to 60−100 μV K^{-1} for $x = 0.8$−1. Despite degenerate conduction, S remains relatively high, $S = 100$ μV K^{-1} for $x = 0.8$ at 300 K. This relatively high value of S should to be attributed to existence of Fe^{2+}/Fe^{3+} with correlation of 3d electrons. In a

dx.doi.org/10.1021/ic401310c | Inorg. Chem. 2013, 52, 9861−9866

strong correlation system, it is reported that the S might be enhanced by the spin and orbital degree of freedom.[46,47] Figure 6c shows κ versus T. The value of κ at 300 K is in the range 10^{-3}–10^{-2} W cm^{-1} K^{-1} for all samples. Figure 6d shows ZT versus T. The sample with $x = 0.8$ indicates a maximum ZT value of 0.044 at 300 K, which is mainly because of the low ρ of the $x = 0.8$ sample.

DISCUSSION

The oxide impurity, SnO_2, in $x = 0$–0.6 samples is unexpected in dry syntheses, although it has also been observed in the literature.[32] The presence of SnO_2 should to be ascribed to the transition from unstable SnS. Tin monosulfide SnS undergoes a second-order phase transition from *Pnma* structure (α-SnS) to *Cmcm* structure (β-SnS) at 605 °C.[48,49] In this study, the sample in evacuated silica tube is quenched from 750 °C, which allows the existence of β-SnS. The unstable β-SnS containing Sn^{2+} may undergo a transition to a more stable SnO_2 containing Sn^{4+} during sample grinding in atmospheric air.

Stannite–kesterite single crystals quenched at 750 °C also have anion defects.[38] In addition, similar chemical composition dependence of ratio of lattice parameter ($c/2a$) is observed in both solid solutions. The disorder process of stannite–kuramite solid solutions, however, differs so much from that of stannite–kesterite. The Sn^{4+} of stannite–kuramite takes part in disorder on the 4*d* and 2*b* sites in all samples, whereas that of stannite–kesterite does not take part in cation exchange and remains on the 2*b* site.[30]

The $x = 1$ sample has values of *a*, *c*, *r*, and Cu/Sn disorder similar to those of tetragonal Cu_2SnS_3, which has a unit cell formula $Cu_{2.665(7)}Sn_{1.335(7)}S_4$, although Cu_2SnS_3 has shorter *r* of 2*a* site, $r_{2a\text{-}S} \approx 0.2307(1)$ nm.[50]

Dimetal chalcogenide $AgBiSe_2$ exhibits fairly good thermoelectric properties at high-temperature cubic phase containing cation disorder.[53,54] Our results indicate that Cu-rich samples with lower anistropy and cation disorder have maximam ZT value, similar to the case of $AgBiSe_2$. These findings strongly suggest a promising strategy in thermoelectrics to focus on the material with mixed occupation and/or antisite disorder.

Figure S4 shows the isotropic atomic displacement parameter (U_{iso}) versus *x*. Some U_{iso} on 2*a* site has unusually large value, for instance, $U_{iso} = 6.62(30) \times 10^{-4}$ and $7.21(30) \times 10^{-4}$ nm^2 for $x = 0.2$ and 0.4, respectively. As shown in Figure S5, the κ at 300 K versus *x* exhibits behavior similar to that of U_{iso} on 2*a* site. This result suggests that the κ is sensitive to thermal vibration of 2*a* site, as well as crystal structure and chemical composition, although large U_{iso} generally suppresses the κ.[51] A slight increase of κ at 300 K of $x = 0.8$–1 comes from a decrease of ρ, degenerate conduction.

The κ value of all samples is much lower than that of sphalerite (ZnS), 0.27 W cm^{-1} K^{-1}.[52] This can be mainly attributed to phonon scattering by the highly distorted crystal structure, cation disorder, and anion defects. The $x = 0.8$ sample has larger ZT value ($\rho = 4.9$ mΩ cm, $S = 100$ μV K^{-1}, $\kappa = 0.014$ W cm^{-1} K^{-1}, and $ZT = 0.044$) than that of $Cu_2Zn_{0.90}In_{0.10}SnSe_4$ ($\rho = 3.4$ mΩ cm, S = 75 μV K^{-1}, $\kappa = 0.035$ W cm^{-1} K^{-1}, and $ZT = 0.014$) at 300 K because of large *S* and low κ.[13] As shown in Figure 6, the ZT values of all samples show an increase with T, indicating that a higher ZT of these samples might be achieved at higher temperatures.

Although $Cu_{2+x}Fe_{1-x}SnS_{4-y}$ ($x = 0.8$–1) exhibits degenerate conduction, the existence of anion defects and cation disorder complicates the carrier doping mechanism. Furthermore, pure kuramite has been reported to crystallize in the cubic $F\bar{4}3m$ space group.[55] Our results suggest that a detailed structural and electronic phase diagram of Cu_3SnS_{4-y} is essential for verifying the structural and electronic properties of the Cu_2–II–IV–VI_4 group.

CONCLUSIONS

The structural and thermoelectric properties of polycrystalline $Cu_{2+x}Fe_{1-x}SnS_{4-y}$ ($x = 0$–1) have been elucidated. Sulfur defects (y) are inevitable in $Cu_{2+x}Fe_{1-x}SnS_{4-y}$ ($x = 0.2$–1). The amount of y is estimated to be a maximum of ∼10 mol % for $x = 1$. Structural anisotropy decreases with *x*, which results in the ratio of the lattice constants ($c/2a$) to be ∼1 and the convergence of bond length. The Cu/Sn disorder increases with *x*. The samples with $x = 0$–0.7 have $d\rho/dT < 0$, and the activation energy (E_a) is calculated as 0.02–0.05 eV, whereas the samples with $x = 0.8$–1 exhibit degenerate conduction. The value of S still remains relatively high despite degenerate conduction, $S \approx 100$ μV/K for $x = 0.8$ at 300 K. The κ values of the solid solutions are in the range 10^{-3}–10^{-2} W cm^{-1} K^{-1}, and ZT reaches 0.044 for $x = 0.8$ at 300 K, which is doubly larger than that of $x = 0$. These results indicate that a higher ZT value could be achieved through the optimization of the chemical composition.

ASSOCIATED CONTENT

Supporting Information

Table S1 shows chemical composition of the samples obtained using EPMA analyses. Figure S1 shows anomalous scattering factors versus wavelength of Cu and Fe. Figure S2 shows powder XRD patterns of $Cu_{2+x}Fe_{1-x}SnS_{4-y}$ ($x = 0.1$–0.9) and the results of the Rietveld analysis. Figure S3 shows SEM images of $Cu_{2+x}Fe_{1-x}SnS_{4-y}$ ($x = 0.1$–0.9). Figure S4 shows the isotropic atomic displacement parameter of $Cu_{2+x}Fe_{1-x}SnS_{4-y}$. Figure S5 shows thermal conductivity at 300 K for $Cu_{2+x}Fe_{1-x}SnS_{4-y}$. This material is available free of charge via the Internet at http://pubs.acs.org.

AUTHOR INFORMATION

Corresponding Author

*E-mail: 60508588@z8.keio.jp.

Notes

The authors declare no competing financial interest.

ACKNOWLEDGMENTS

We thank Mr. J. C. Lee (Central Service Facilities for Research in Keio University) for help in EPMA measurement. This work was partially supported by research grants from Keio University, the Keio Leading-edge Laboratory of Science and Technology (KLL), and Funding Program for World-Leading Innovative R&D on Science and Technology (FIRST) from the Japan Society for Promotion of Science (JSPS).

REFERENCES

(1) Seebeck, T. J. In *Magnetische Porarisation der Metalle und Erze durch Temperature-Differenz*; Oettingen, A., Ed.; Wilhelm Engelmann: Leipzig, 1895.

(2) Thomson, W. *Mathematical and Physical Papers*; Cambridge Press: London, 1882; Vol. *1*, p 232 [Trans. R. Soc. Edinb. Vol. XXI, Pt. I, 1854].

(3) Rockwood, A. *Phys. Rev. A* **1984**, *30*, 2843.

(4) Mahan, G. D.; Sofo, J. O. *Proc. Natl. Acad. Sci. U.S.A.* **1996**, *93*, 7436.

(5) Slack, G. A. In *CRC Handbook of Thermoelectrics*; Rowe, D. M., Ed.; Chemical Rubber: Boca Raton, FL, 1995; p 407.

(6) Sales, B. C.; Mandrus, D.; Williams, R. K. *Science* **1996**, *272*, 1325.
(7) Nolas, G. S.; Cohn, J. L.; Slack, G. A.; Schulman, S. B. *Appl. Phys. Lett.* **1998**, *73*, 178.
(8) Caillat, T.; Fleurial, J. P.; Borshchevsky, A. *J. Phys. Chem. Solids* **1997**, *58*, 7.
(9) Snyder, G. J.; Christensen, M.; Nishibori, E.; Caillat, T.; Iversen, B. B. *Nat. Mater.* **2004**, *3*, 458.
(10) Terasaki, I.; Sasago, Y.; Uchinokura, K. *Phys. Rev. B* **1997**, *56*, 20.
(11) Zhao, L. D.; Berardan, D.; Pei, Y. L.; Byl, C.; Pinsard-Gaudart, L.; Dragoe, N. *Appl. Phys. Lett.* **2010**, *97*, 092118.
(12) Liu, H.; Shi, X.; Xu, F.; Zhang, L.; Zhang, W.; Chen, L.; Li, Q.; Uher, C.; Day, T.; Snyder, G. J. *Nat. Mater.* **2012**, *11*, 422.
(13) Shi, X. Y.; Huang, F. Q.; Liu, M. L.; Chen, L. D. *Appl. Phys. Lett.* **2009**, *94*, 122103.
(14) Liu, M. L.; Chen, I. W.; Huang, F. Q.; Chen, L. D. *Adv. Mater.* **2009**, *21*, 3808.
(15) Yang, C.; Huang, F.; Wu, L.; Xu, K. *J. Phys. D: Appl. Phys.* **2011**, *44*, 295404.
(16) Ibáñez, M.; Zamani, R.; LaLonde, A.; Cadavid, D.; Li, W.; Shavel, A.; Arbiol, J.; Morante, J. R.; Gorsse, S.; Snyder, G. J.; Cabot, A. *J. Am. Chem. Soc.* **2012**, *134*, 4060.
(17) Katagiri, H. *Thin Solid Films* **2005**, *480*, 426.
(18) Brockway, L. O. *Z. Kristallogr.* **1934**, *89*, 434.
(19) Moh, G. H. *N. Jb. Miner. Abh.* **1960**, *94*, 1125.
(20) Moh, G. H.; Ottemann, J. *N. Jb. Miner. Abh.* **1962**, *99*, 1.
(21) Nitsche, R.; Sargent, D. F.; Wild, P. *J. Cryst. Growth* **1967**, *1*, 57.
(22) Schäfer, W.; Nitsche, R. *Mater. Res. Bull.* **1974**, *9*, 645.
(23) Teske, C. L. *Z. Anorg. Allg. Chem.* **1976**, *419*, 67.
(24) Teske, C. L. *Z. Naturforsch.* **1979**, *34b*, 386.
(25) Guen, L.; Glaunsinger, W. S. *J. Solid State Chem.* **1980**, *35*, 10.
(26) Tampier, M.; Johrendt, D. *Z. Anorg. Allg. Chem.* **2001**, *627*, 312.
(27) Kovalenker, V. A.; Evstigneeva, T. L.; Troneva, N. V.; Vyal'sov, L. N. *Zap. Vses. Miner. Obsh.* **1979**, *108*, 564.
(28) Fleisher, M.; Cabri, L.; Chao, G. *Am. Mineral.* **1980**, *65*, 1065.
(29) Bonazzi, P.; Bindi, L.; Bernardini, G. P.; Menchetti, S. *Can. Mineral.* **2003**, *41*, 639.
(30) Schorr, S.; Hoebler, H. J.; Tovar, M. *Eur. J. Mineral.* **2007**, *19*, 65.
(31) Evstigneeva, T. L.; Rusakov, V. S.; Kabalov, Y. K. *New Data Mineral* **2003**, *38*, 65.
(32) Rusakov, V. S.; Chistyakova, N. I.; Burkovsky, I. A.; Gapochka, A. M.; Evstigneeva, T. L. *Bull. Russ. Acad. Sci. Phys.* **2010**, *74*, 389.
(33) Zalewski, W.; Bacewicz, R.; Antonowicz, J.; Pietnoczka, A.; Evstigneeva, T. L.; Schorr, S. *J. Alloys Compd.* **2010**, *492*, 35.
(34) Kissin, S. A. *Can. Mineral.* **1989**, *27*, 689.
(35) Benedetto, F.; Di Gatteschi, D. *Phys. Chem. Miner.* **2000**, *27*, 453.
(36) Izumi, F.; Momma, K. *Solid State Phenom.* **2007**, *130*, 15.
(37) Momma, K.; Izumi, F. *J. Appl. Crystallogr.* **2011**, *44*, 1272.
(38) Bernardini, G. P.; Bonazzi, P.; Corazza, M.; Corsini, F.; Mazzetti, G.; Poggi, L.; Tanelli, G. *Eur. J. Mineral.* **1990**, *2*, 219.
(39) Zeier, W. G.; Pei, Y.; Pomrehn, G.; Day, T.; Heinz, N.; Heinrich, C. P.; Snyder, G. J.; Tremel, W. *J. Am. Chem. Soc.* **2013**, *135*, 726.
(40) Cromer, D. T.; Liberman, D. *J. Chem. Phys.* **1970**, *53*, 1891.
(41) Sasaki, S. *KEK Rep.* **1989**, *88*, 14.
(42) Brown, I. D.; Altermatt, D. *Acta Crystallogr.* **1985**, *B41*, 244.
(43) (a) The BVS of i site (BVS_i) was calculated as $BVS_i = \sum_{(j=Fe,Cu,Sn)} g_j BVS_j$. The BVS_j was calculated using the following parameters: $b_0 = 0.37$ for all atoms, $r_0 = 2.125$ for Fe, $r_0 = 1.898$ for Cu, and $r_0 = 2.339$ for Sn. (b) Brese, N. E.; O'Keeffe, M. *Acta Crystallogr.* **1991**, *B47*, 192.
(44) Eibschütz, M.; Hermon, E.; Shtrikman, S. *J. Phys. Chem. Solids* **1967**, *28*, 1633.
(45) Cutler, M.; Leavy, J. F.; Fitzpatrick, R. L. *Phys. Rev.* **1964**, *133*, A1143.
(46) Koshibae, W.; Tsutsui, K.; Maekawa, S. *Phys. Rev. B* **2000**, *62*, 6869.
(47) Koshibae, W.; Maekawa, S. *Phys. Rev. Lett.* **2001**, *87*, 236603.
(48) Wiedemeier, H.; Csillag, F. J. *Z. Kristallogr.* **1979**, *149*, 17.
(49) Burton, L. A.; Walsh, A. *J. Phys. Chem. C* **2012**, *116*, 24262.
(50) Chen, X.; Wada, H.; Sato, A.; Mieno, M. *J. Solid State Chem.* **1998**, *151*, 144.
(51) Sales, B. C.; Chakoumakos, B. C.; Mandrus, D.; Sharp, J. W. *J. Solid State Chem.* **1999**, *146*, 528.
(52) Slack, G. A. *Phys. Rev. B* **1972**, *6*, 3791.
(53) Xiao, C.; Qin, X.; Zhang, J.; An, R.; Xu, J.; Li, K.; Cao, B.; Yang, J.; Ye, B.; Xie, Y. *J. Am. Chem. Soc.* **2012**, *134*, 18460.
(54) Xiao, C.; Xu, J.; Cao, B.; Li, K.; Kong, M.; Xie, Y. *J. Am. Chem. Soc.* **2012**, *134*, 7971.
(55) Di Benedetto, F.; Borrini, D.; Caneschi, A.; Fornaciai, G.; Innocenti, M.; Lavacchi, A.; Massa, C. A.; Montegrossi, G.; Oberhauser, W.; Pardi, L. A.; Romanelli, M. *Phys. Chem. Miner.* **2011**, *38*, 483.